Al-Rafidain Journal of Engineering Sciences

Journal homepage https://rjes.iq/index.php/rjes

ISSN 3005-3153 (Online)

Experimental Configuration and Operating Parameters of the Thermo-Fluid Energy Conversion System

Salam Abid Muslim Abd Ali

Department of Mechanical Engineering, Faculty of Engineering, Islamic Azad University, Tehran, Iran,

ARTICLE INFO

Article history:

Received	3 February 2026
Revised	3 February 2026
Accepted	13 February 2026
Available online	13 February 2026

Keywords:

Thermo-fluid energy conversion;
Fluidized sand reactor;
Thermoelectric generation;
Energy recovery;
Experimental investigation

ABSTRACT

The present experimental investigation describes an optimization of thermo-fluid energy conversion through the design of a compact sand-fluidized reactor with controlled air heating and interchangeable inlet geometries. The system includes a TEC1-12706 thermoelectric module for thermal conditioning, an air pump at variable speed, a transparent acrylic column filled with silica sand, and a small electrical generator for energy recovery. Effects of air velocity (0.5–1.5 m/s), temperature setpoint (30–90 °C), sand mass (100–300 g), and inlet geometry (Straight, Ring, V-shape) were examined systematically through a full factorial design with 81 operational conditions. The electrical power output, pressure drop, and thermal-to-electrical conversion efficiency were evaluated under steady-state operation. It has emerged from the results that inlet geometry has a decisive influence on hydrodynamic characteristics and energy performance. The Ring inlet always exhibited better flow uniformity with the most electrical power at (~3.5 W) at 1.5 m/s and 90 °C and a lower pressure drop (~450 Pa) than the Straight (~560 Pa) and V-shape (~660 Pa) configurations. Maximum thermal-to-electrical performance occurred in the range of 27–28% in the hot airflow and temperature situations that occurred through the Ring inlet. Improving air velocity improved mean efficiency from 7–8% at 0.5 m/s to nearly 16–17% at 1.5 m/s, while raising temperature from 30 to 90 °C increased average efficiency from approximately 9–10% to 16%. Sand mass had a relatively non-monotonic effect at 200 g, giving peak average efficiency of approximately (13.6%): Lower and higher masses presented low performance due to lower thermal contacts as well as higher pressure losses, respectively. In general, the Ring inlet exhibited a better electrical output than the Straight inlet, increasing the electrical output by some 25% under the same conditions of the Straight as a whole, indicating how crucial inlet design is for coupled thermo-fluid systems. This concept of the optimal operating window – high airflow, high temperature, and moderate sand loading – serves as a practical guideline to design compact energy recovery devices with fluidized granular media.

1. Introduction

Due to the global demand for sustainable energy systems, research on the recovery and conversion of low- to medium-grade thermal energy has increased. The significant untapped energy resource of waste heat released daily from industrial processes, ventilation systems, and compact thermal devices. These thermal energy distributed widely throughout the plant will be required for their effective conversion into usable electrical power as they need small, low-cost, and versatile technologies to operate on mild-temperature scale and varied flow condition. Thermo-fluid energy conversion systems that integrate forced convection, granular media, and thermoelectric production have drawn increasing attention among these methods. Such systems employ fluid flow not only as a heat carrier but also as a dynamic agent for improved heat transfer due to a combination of particle agitation and mixing. Fluidized or semi-fluidized granular beds, in particular, present greater effective surface

Corresponding author E-mail address: engineeroil9@gmail.com
https://doi.org/10.61268/yhg4cc67

area, better thermal homogenization, and inherent thermal storage capacity. Such properties ensure sand-based reactors appeal toward the compact processing process for energy harvesting purposes, if they are coupled with thermoelectric modules, that can convert temperature difference into electrical energy directly. The hydrodynamic profile of the inlet region profoundly influences distribution of flow, suspension of particles, pressure losses, and the thermal performance. Inefficient inlet design results in flow channeling, localized jets, and stagnant zones, which negatively affect heat transfer and conversion efficiency. Optimized inlet geometries, on the other hand, can facilitate uniform fluidization, can reduce dead zone conditions, and improve the convective velocity of the fluid. Inlet geometries, despite their significance, are often considered to be a secondary design parameter, which is little examined experimentally and comprehensively for comparison purposes concerning effects on coupled thermo-fluid and electrical characteristics, specifically on small laboratory scale systems. Simultaneously the variables which affect the operational performance of the system include airflow velocity, inlet temperature, granular loading, which influence system behavior. Increasing flow velocity usually increases the particle motion and the heat transfer at the cost of higher pressure loss and the pumping force. The thermoelectric driving force increases with higher temperature, the particle mass is responsible for the trade-off between thermal storage capability and hydrodynamic resistance. Therefore, the determination of the best combination of the mentioned parameters is very important for efficient energy recovery.

(Abdelmagied, 2024) [1] studied the thermo-fluid properties and exergy performance of twisted tube helical coils by showing significant improvement in heat transfer and moderate pressure penalties. For which the secondary swirling flow plays an important role in decreasing irreversibility (and hence improving the thermal efficiency) overall. (Abdelrehim et al., 2024) [2] experimental investigation of wick-absorbent designs in solar stills to observe substantial productivity improvements due to enhanced capillary effects and evaporation. The authors conclude their results showed that optimized wick geometry improves thermal utilization and increases freshwater yield. (Acharya et al., 2025) [3] investigated spring-fin turbulators mounted on solar air heater absorber plates, and reported substantial improvement in Nusselt number with acceptable friction factor rise. And fin placement strongly affected flow disruption and boundary-layer thinning according to the authors. (Agati et al., 2024) [4] carried out thermo-fluid dynamic simulations of airflow in an indoor vertical farming system that demonstrated non-uniform temperature-velocity distributions in the airflows in indoor vertical farming systems. They offer design guidelines on how to achieve a homogeneous microclimate and increasing crop temperature comfort with the use of thermoclimatic principles. (Alrashidi et al., 2025) [5] investigated their own hydrogel-based PV cooling under different operating conditions and found significant reduction in module temperatures with corresponding electrical efficiency improvements. The investigation validated hydrogels as a cheap passive cooling product for photovoltaic systems. (Atiqur Rahman et al., 2025) [6] investigated tubular heat exchangers with opposite-oriented trapezoidal wing perforated baffles, obtaining high heat transfer augmented. The perforation geometry balances turbulence formation and pressure loss well according to their results. (Baccoli et al., 2025) [7] constructed (linear and nonlinear) models of a thermoacoustic electric generator run on waste heat and confirmed its performance by experimentation. They showed that we could turn low-grade heat into electricity with a decent level of conversion efficiency. (Behzad et al., 2025) [8] performed a multi-objective optimization of honeycomb absorbers for concentrated solar power systems for simultaneous thermal efficiency and structural integrity. Their framework determined suitable cell geometries that reduce thermal stress while enhancing absorption. (Bianco et al., 2023) [9] introduced a CFD-mediated optimization approach for

PCM-assisted heat recovery ventilation elements to demonstrate high levels of energy savings and indoor thermal regulation improvement. The findings emphasized the need for coupling phase change dynamics and airflow modeling. (Catalán-Martínez et al., 2022) [10] modeling the thermo-fluid response in tubular proton-conducting steam electrolysis cells showed strong coupling of temperature fields with electrochemical performance. Their study explored heat management approaches for high-temperature hydrogen production. (Claussner et al., 2025) [11] studied the thermo-fluid dynamics of liquid hydrogen storage and transfer, focusing on thermal stratification and boil-off. The research introduced forecasting tools to reduce exergy destruction in cryogenic hydrogen systems. In their study, (Dhaundiyal & Atsu, 2022) [12] explored the effect of air thermo-fluid properties on the solar collector properties, showing that both the temperature-dependent viscosity and density have strong effects on the solar collector's efficiency. They stressed this to improve accuracy in the property modelling of solar thermal simulations. (Di Meglio & Massarotti, 2022) [13] examined CFD modeling of thermoacoustic energy conversion, noting how turbulence and acoustic coupling are currently limited. They also presented potential avenues for better numerical fidelity in thermoacoustic devices. (Di Meglio et al., 2024) [14] have experimentally established a heat exchanger model for thermoacoustic applications that correlates closely with the simulation-measurement results. Their results reinforced the credibility regarding the design of oscillatory thermal systems based on CFD. (Fu et al., 2025) [15] introduced embedded microchannel cooling systems for high-power electronics to achieve significant reductions in junction temperatures by designing microchannel cooling methods for power electronics devices. From the study the analysis presented here showed that the micro-scale flow control in semiconductor thermal management of the next generation is crucial. (Guille et al., 2026) [16] evaluates the thermo-fluid and economic performance of printed circuit heat exchangers in high-temperature thermal storage, with sCO_2 Brayton cycles. They found increased system efficiency and a favorable cost-performance tradeoff. (Jiao et al., 2024) [17] highlighting synergistic effects of fluid transport and charge generation in the development of 3D materials-based hydrovoltaic generators. Their work put hydrovoltaics at the vanguard of hybrid energy harvesting.(Kwasi-Effah et al., 2024) [18] examined novel TPMS geometries for thermo-hydraulic systems and showed significantly higher heat transfer than conventional channels. However, this study highlighted the geometric freedom of TPMS architecture in condensed heat exchanger design. (Mezzacapo et al., 2025) [19] simulated slot-jet impingement with generalized turbulence models that represented detail of heat transfer at local heat transfer behaviour. The results highlight the sensitivity of impingement cooling to turbulence closure pick. (Persico et al., 2024) [20] built a thermo-fluid model of a supercritical CO_2 compressor for waste heat recovery, indicating strong relationship between the real gas and the aerodynamics. These results supported sCO_2 cycles as a promising choice for high efficiency recovery system. (Rahman, 2024b) [21] presented conical perforated flow deflectors in tubular heat exchanger, improving thermal performance along with a controlled pressure drop. The proposed method focused on perforation for optimizing flow mixing. (Rahman, 2024a) [22] also studied the concept of axially perforated rectangular baffle plates, showing better thermo-fluid properties than traditional plates. Axial perforation induces uniform velocity fields, and therefore, reduced dead zones, as demonstrated by the author. (Rostami & Ahmadi, 2025) [23] explored the importance of pipe design in order to improve thermo-fluid behavior and prevent exergy-induced destruction in heat exchangers. They showed geometric optimization can reduce irreversibility while improving heat transfer. (Sahrane & Niou, 2025) [24] compared turbulence models for shell-and-tube heat exchangers with combined tube bundles and found that there are mainly models which predict temperature and pressure fields best.

Their investigation thus gave practical guidance on how best to apply CFD. (Sarkar, 2024) [25] applied computational thermo-fluid dynamics concepts to both hydrogen-integrated industrial heat systems as well as hydrogen-combined process improvement programs for heat reduction. The paper spotlighted the part of CFD to support sustainable industrial energy transitions. (Shimada et al., 2024) [26] have studied evaporative heat transfer in a porous porous material in an additively manufactured structure, connecting observed thermo-fluid characteristics to increased performance. Their results confirmed AM porosity as a promising asset for increasing phase-change enhancement. (Starace et al., 2021) [27] compared circular and elliptical tubes in evaporative condensers, and found better heat transfer for elliptical geometries that had reduced wake segments. Shape optimization used as passive enhancement technique in the study. (Toor et al., 2026) [28] studied rooftop vertical axis wind turbines, optimizing its core design and gaining increased aerodynamic efficiency through this study experimentally and numerically. Their integrated CFD–experimental methodology proved the feasibility of sustainable urban wind technologies. (Xiao et al., 2025) [29] also constructed coupled- thermo-fluid–solid models for wet milling Al6061 and measured its parametric effect on surface integrity. The study showed that both process temperature and flow strongly determine material quality.

This research aims to perform an experiment of thermo-fluid energy conversion in a compact sand-fluidized reactor coupled with thermoelectric generation, focusing on the effect of the inlet geometry. By varying air velocity, temperature setpoint, sand mass, and inlet configuration to experimentally assess which operating modes can maximize electrical power output and thermal-to-electrical efficiency, and minimize pressure losses. Aim: The ultimate goal is to develop feasible designs for small-scale energy recovery systems to be applied on an end-user application scale using granular media. While fluidized granular systems and thermoelectric devices have been well-investigated separately, little experimental work has investigated their joint use for compact reactors with very limited inlet geometries. For instance, comparisons between Straight, Ring, and V-shape inlets at the same thermo-fluid conditions are still limited. Additionally, the majority of studies have included only hydrodynamics or thermal performance and have reported only integrated pressure drop, electrical power generation, and conversion efficiency results from the same laboratory experiment. The key work proposed in this paper is the empirical synthesis of a sand-fluidized mini-reactor based on thermoelectric energy harvesting and interchangeable 3D-printed inlet geometries. A full factorial parametric analysis is carried out to measure the impact of airflow velocity, temperature, particle loading, and inlet configuration towards hydrodynamic losses and electrical power. Thus, this work presents the first systematic empirical comparison of Ring, Straight, and V-shape inlets in a thermo-fluid energy conversion system, and reveals optimal operating windows and shows that optimizing the inlet can increase electrical power by more than 25%.

2. Experimental work

This was the experimental research to study the coupled thermo–fluid dynamic behavior and energy conversion performance of the sand-based mini fluidized reactor and a thermoelectric generator. It is built up with a vertically mounted transparent acrylic column (inner diameter 25 mm and height 250 mm), and covered with silica sand at controlled masses of 100, 200 and 300 g, which can be supplied from the bottom by a variable-speed air pump to inlet velocities of 0.5, 1.0 and 1.5 m/s regulated with a digital flowmeter. A thermal energy is presented by a TEC1-12706 thermoelectric module that is attached to an aluminum heat-sink assembly with predetermined temperature setpoints at 30, 60 and 90 °C. Three interchangeable inlet geometries (Straight, Ring, and V-shape) were 3D printed using PLA and fabricated, and

attached to columns at the bottom, to evaluate their effects on flow distribution, sand fluidization, pressure drop, and thermal-to-electrical efficiency. Circumferential injection of air to the Ring inlet, axial flows to the Straight inlet, and inclined jets and improved turbulence to the V shape inlet. The air flows up from the bottom and out from above, providing upward motion of particles and internal mixing. Temperature sensors were fitted inlet and outlet locations to monitor the temperature gradients to check thermal gradients, differential pressure sensors were installed to find loss pressure across the sand bed. The output of the thermoelectric module was continuously logged and their electrical output was monitored to calculate the power generated from power and the energy conversion efficiency. All the experiments were performed all kept at steady state from the original state after stabilization of the thermal regime. For each layout, parametric sweeps were performed by varying air velocity, temperature setpoint, sand mass, and inlet geometry separately and without touching the rest. All tests were performed in multiple replicates for repeatability, and averaged values were analyzed. Each main effect and interactions among hydrodynamic forcing, thermal input, particle loading, and inlet design were systematically evaluated using the experimental matrix. The methodology allows a holistic approach to calculate the manner in which the flow structure and bed dynamics determine the enhancement of heat transfer and electrical energy production in highly compact thermo-fluid systems under regulated conditions of heat transfer.

2.1 Main Components of the Experimental System

The experimental system comprises multiple integrated subsystems enabling controlled transformation of thermo-fluid energy from sand fluidization. A variable-speed air pump delivers the air, and the inlet can be adjusted to velocities of 0.5, 1.0, and 1.5 m/s, which is the driving source for the working fluid and a means to control the hydrodynamic status in the reactor. The pumped air is directed to a TEC1-12706 thermoelectric (Peltier) module coupled with a special aluminum heat-sink structure that acts like a small heat exchanger. This unit sets regulated thermal threshold levels of 30, 60, and 90 °C, which allows for a required thermal gradient for thermoelectric power generation at the same time, and helps condition inlet airflow. Downstream of the thermal unit, it goes through a digital flowmeter, that measures in time the volumetric velocity to optimize velocity control. Temperature sensors are also mounted at specific sites, such as the reactor's inlet and outlet, to measure thermal gradient in the sand bed and heat transfer effectiveness, as well as heat transfer efficiency. These sensors offer real-time temperature readings to generate the response needed to calculate the thermal-to-electrical efficiency. The airflow, which is controlled by air, then enters the acrylic reactor column thru interchangeable inlet geometries 3D printed as plastic and PLA filament (see Appendix M with interchangeable inlet geometries) of variable length. Straight, ring and V shapes are discussed three inlet form. These geometries control the flow vector and directly affect particle suspension, mixing characteristics and pressure loss. The actual reactor is a transparent acrylic tube (an inner diameter of 25 mm and a height of 250 mm), and as such, can be observed visually in terms of patterns of sand fluidized. Silica sand is used as the porous medium and thermal storage material inside the column, with 100, 200, and 300 g masses to study the effects of particle loading. At the reactor outlet, the increased airflow activates a miniaturized electric generator, which transfers component kinetic energy into electrical power, augmenting the thermoelectric output. The resulting voltage and current are measured to work out the net electrical power. All internal connections are fabricated with 6 mm plastic tubing to reduce heat loss and flow resistance. Consequently, they make up a small experimental set-up, facilitating a systematic investigation of coupled airflow dynamics, particle behavior,

heat transfer, and electrical energy generation under different operating conditions.

Figure 1. Miniature Air-Driven Electrical Generator Used for Kinetic Energy Recovery

Figure 2. TEC1-12706 Thermoelectric Module Integrated with Aluminum Heat Sink and Cooling Fan

Figure 3. Aluminum air heating Block Used as Compact Heat Exchanger for Thermal Conditioning

Figure 4. Variable-Speed Mini Air Pump with Integrated Micro Solenoid Valve

Figure 5. Digital Flow Meter for Real-Time Airflow Measurement

Figure 6. K-Type Thermocouple Temperature Sensor for Inlet and Outlet Thermal Monitoring

Figure 7. Transparent Acrylic Tubes Used as Reactor Columns for Sand Fluidization

Figure 8. Three-Dimensional Printed Inlet Geometries (Straight, Ring, and V-Shape) Fabricated in PLA for Flow Distribution Control

2.2 *System Integration and Experimental Procedure*

Figure 9 The schematic flowchart of the whole system is shown here to show the thermal conditioning, airflow regulation, sand fluidizing, and energy harvesting subsystem integration. It starts with an external power supply feeding the TEC1-12706 Peltier module, setting controlled air heating to predetermined temperature levels of 30, 60, and 90 °C. At the same time, a variable-speed air pump drives the airflow down a length of 6 mm plastic tubing toward the measurement area. The air initially enters through a digital flow meter which can be monitored and inlet velocities (0.5, 1.0 and 1.5 m/s) adjusted in real time. After flow regulation, a temperature sensor in the inlet monitors the conditioned air temperature before entering the interchangeable inlet geometries. The airflow is either directed toward one of three 3D-printed inlet (Straight, Ring, or V-shape) configurations according to the design of the experimental site, which are responsible for spatial distribution and momentum of the injected air. The conditioned flow of airflow then feeds into the acrylic reactor column (25 mm diameter, 25 cm height), containing silica sand of specified masses of 100, 200 or 300 g, where the upward flow causes particle suspension and internal mixing and a dense fluidized bed that enables convective heat transfer and thermal storage. From the reactor outlet, the supercharged air stream flows through a mini hydro-type electrical generator, which turns some of the kinetic energy into electrical power. An outlet temperature sensor detects the exhaust air temperature for the extraction and analysis of thermal extraction along the sand bed. Electrical signals from the generator, flow rate, and temperature data are then transmitted to Arduino to gain data that are measured using the data acquisition unit. All sensor outputs are synchronized and are recorded in real time, with the data saved on a PC or SD card for post processing. With a parameter (air velocity, temperature, sand mass, or inlet geometry) varying at each experimental run and the other parameters remaining constant. Measurements were recorded after stabilizing to a steady state to make sure that we ensure repeatability and stability. This integrated method not only permits the simultaneous measurement of such hydrodynamic behavior as thermal transport and electrical power generation, but also offers a comprehensive platform for analyzing co-joint mechanisms of the conversion of thermo-fluids into energy.

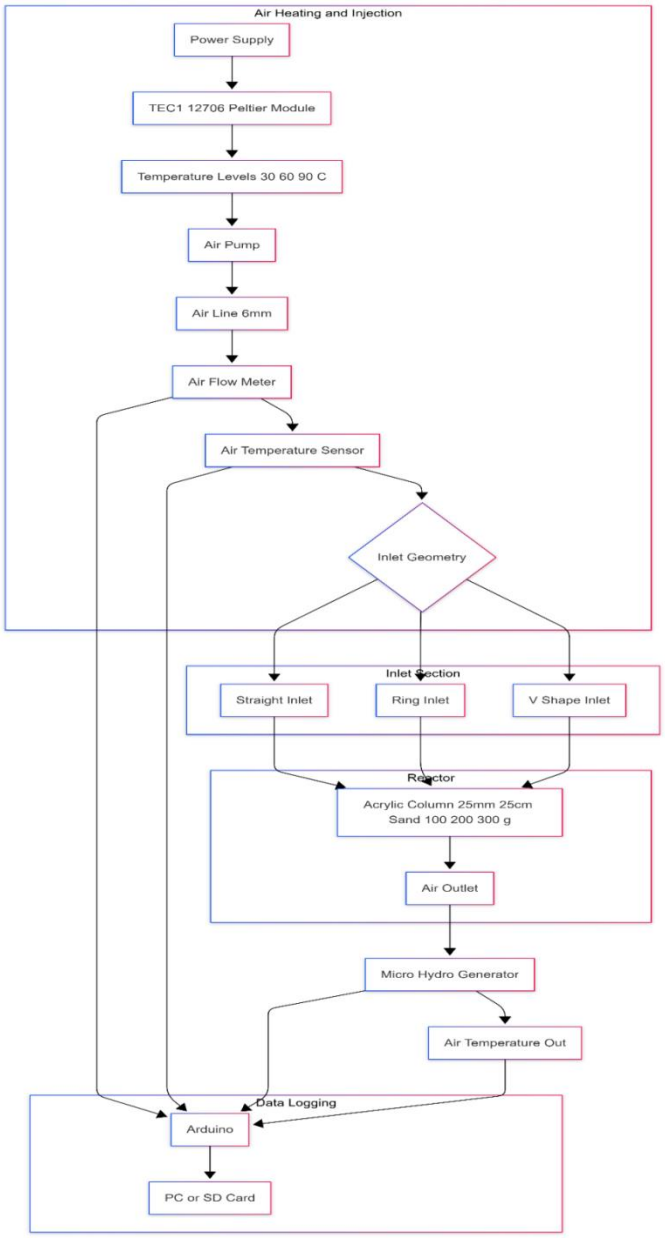

Figure 9. Schematic Flowchart of the Integrated Experimental System for Air Heating, Sand Fluidization, and Energy Conversion

2.3 Measurement Procedure and Experimental Cases

The experimental measurements were carried out in accordance with a systematic parametric approach to determine the effect of airflow velocity, inlet temperature, sand mass, and inlet geometry on thermo-fluid and energy conversion performance of the system. For all the experiments, the desired temperature setpoint (30, 60, or 90 °C) was selected by the TEC1-12706 thermoelectric module, and then maintained until thermal steady state was achieved. After which the speed of the air pump was set to obtain the required inlet velocity (0.5, 1.0, or 1.5 m/s) as verified by a digital flow meter. After both the thermal conditions and hydrodynamic conditions were stable, silica sand was loaded into the acrylic reactor at fixed masses (100, 200, or 300 g), after which the inlet geometry (Straight, Ring, or V-shape) was chosen. For each configuration, inlet air temperature, outlet air temperature, volumetric flow rate, and micro-generator electrical output were continuously measured by calibrated sensors interfaced with an Arduino-based data acquisition system. At

steady operation, usually after about a few minutes, measurements were made over a defined sampling time, taking into account transient fluctuations. Each experimental increment was repeated at least three times to obtain repeatability across the series and is then represented by the reported values and averaged with respect to those measurements. The experimental matrix was designed from the 81 operating cases obtained from three air velocities (3 levels), three temperature system setpoints (3 levels), three sand masses (3 levels), and three inlet geometries (3 levels), i.e., 3×3×3×3=81 test conditions. This elaborate dataset allowed testing of individual parameters and interaction effects with thermal input, hydrodynamic forcing, particle loading, and inlet design. The registered measurements yielded some of the following key performance indicators: pressure drop in the reactor, power generation of the electric system, and thermal-to-electrical conversion efficiency. Additionally, qualitative flow phenomena were observed visually and analyzed the patterns of sand fluidization. These data were used to generate velocity-, temperature-, sand mass-, geometry-dependent performance curves, efficiency heatmaps, three-dimensional response surfaces, and main-effect plots. Such findings offer a comprehensive quantified foundation for selecting optimal operating conditions and evaluating the relative importance of each control parameter in adjusting thermo-fluid energy conversion.

2.4 Governing Equations and Data Reduction

1. Airflow and velocity

Volumetric flow rate (from flow meter):$Q[\ \mathrm{m}^3/\mathrm{s}]$

Superficial air velocity inside the acrylic column:

$$v = \frac{Q}{A_c} \tag{1}$$

Column cross-sectional area:

$$A_c = \frac{\pi D^2}{4} \tag{2}$$

2. Pressure drop across the sand bed

Measured pressure drop:

$$\Delta P = P_{\text{in}} - P_{\text{out}} \tag{3}$$

(If you also report a dimensionless form)
Pressure drop coefficient:

$$C_{\Delta P} = \frac{\Delta P}{\frac{1}{2}\rho v^2} \tag{4}$$

3. Heat (thermal) rate removed from the hot air stream

Using inlet and outlet temperatures measured by thermocouples:
Mass flow rate of air:

$$\dot{m}_a = \rho_a Q \tag{5}$$

Thermal power transferred (air-cooling across

$$\dot{Q}_{\text{th}} = \dot{m}_a c_{p,a}(T_{\text{in}} - T_{\text{out}}) \tag{6}$$

4. Electrical output power

If you measure generator (or TEG) voltage and current:
Electrical power:

$$P_e = VI \tag{7}$$

If you log voltage across a known load:

$$P_e = \frac{V^2}{R} \tag{8}$$

5. Thermal-to-electrical efficiency

Conversion efficiency:

$$\eta = \frac{P_e}{\dot{Q}_{\text{th}}} \times 100\% \tag{9}$$

6. Kinetic power and recovery (if you want to quantify "air → generator" part)

Air kinetic power (based on column area):

$$P_k = \frac{1}{2}\rho_a A_c v^3 \tag{10}$$

Kinetic-to-electric efficiency (generator effectiveness):

$$\eta_k = \frac{P_e}{P_k} \times 100\% \tag{11}$$

7. Dimensionless numbers (optional but strong for a fluids paper)

Reynolds number (based on column diameter):

$$\mathrm{Re} = \frac{\rho_a v D}{\mu_a} \quad (12)$$

(If you need particle Reynolds number)

$$\mathrm{Re}_p = \frac{\rho_a v d_p}{\mu_a} \quad (13)$$

8. Energy balance check (recommended in experiments)

Energy balance residual:

$$\epsilon = \frac{\dot{Q}_{\mathrm{in}} - \dot{Q}_{\mathrm{th}}}{\dot{Q}_{\mathrm{in}}} \times 100\% \quad (14)$$

(Here $\dot{Q}_{\mathrm{in}}$ can be estimated from heater/TEC electrical input if you record it.)

3. Results and discussion

This portion reports some of the experimental study results coming from the sand-fluidized thermo-fluid energy conversion system with different working conditions. The effects of air velocity, inlet temperature, sand mass, and inlet geometry on electrical power generation, pressure drop, and thermal-to-electrical efficiency are analyzed one by one. For both individual main effects and combinations between the parameters, efficiency heatmaps, three-dimensional response surfaces, and statistical main-effect plots are used. Particular attention is given to the performance analysis, comparing the Straight, Ring, and V-shape inlet configurations with respect to flow uniformity, particle fluidization, and energy recovery capability. The findings are explored in physical terms in which reported sand movement characteristics are compared with recorded hydrodynamic losses and electrical output. Such an integrated analysis allows identifying where the operating areas should be optimized and delineates the major mechanisms of heat transfer enhancement and energy conversion in the compact reactor envisaged.

Figure 10 presents the differences in pressure drop with air velocity for the Straight, Ring and V-shape inlets, wherein a nonlinear rise in ΔP is apparent with velocity increase. At the lowest speed of 0.5 m/s, the pressure drop is also small at c. 70 Pa in the Straight inlet, ~55 Pa for Ring inlet and ~85 Pa for the V-shape inlet – there is relatively less resistance towards flow in weaker aerodynamic forcing. As the velocity increased to 1.0 m/s, ΔP changes quickly to around 260 Pa (Straight), 210 Pa (Ring), and 310 Pa (V-shape), indicating more significant inertial impact in the air stream, the better interaction between the flow of air and packed sand. Pressure drop dominates at a velocity of 1.5 m/s, with outputs reaching about 560 Pa for Straight, 450 Pa for Ring, and approximately 660 Pa for V-shape, verifying the quadratic dependence of losses on velocity effects. In terms of physics, the Ring inlet always yields the lower ΔP, as it has an annular flow distribution that maximizes uniform flow entry while minimizing localised jetting and recirculation. The highest pressure losses in V-shape inlet are observed at full air speed due to flow splitting and increased turbulence production at the entrance. Straight inlet is between these two extremes and is a base configuration with moderate resistance. The resulting widen between these curves at higher velocities suggests that aerodynamic loading gradually makes inlet morphology more influential. These findings indicate that the design of the entrance directly influences hydrodynamic losses in the reactor (particularly at high speeds). Thus, although higher velocity increases the effect of fluidization intensity, they also impose a large pressure penalty on the V-shape geometry. Overall, the figure demonstrates the trade-off, where mixing and pumping power increases, resulting in the Ring inlet forming the most hydrodynamically-efficient configuration of the tested range. Figure 11 gives the correlation between air velocity and electrical power produced by the micro-hydro unit in the Straight configuration, Ring arrangement and V-shape configuration. The power obtained at a velocity of 0.5 m/s is quite small, being about 0.8 W for a Straight inlet, 1.0 W for a Ring inlet, and almost 0.85 W for a V-shape inlet, showing that the flow rate limits kinetic energy. The electrical output increases almost linearly (circa 1.75 W [Straight]), (circa 2.2 W [Ring]), and (circa 1.9 W [V-shape]) as the rate increases to 1.0 m/s, leading directly to superior momentum transfer

and better fluid–turbine interaction. At a velocity of 1.5 m/s the power received peaks in the range of approximately 2.8 W for Straight, 3.5 W for Ring and 3.0 W for V-shape, meaning that in terms of energy, increasing flow significantly enhances power generation. Physically, this tendency comes from increases in dynamic pressure and mass flow rate and together raises mechanical energy supplied to the generator. The Ring inlet has the highest electrical output of any geometries as it has the more uniform flow distribution and less entrance losses, enabling the incoming energy to become a more valuable power. Second is the V-shape inlet where they have a stronger mixing but suffer from minor losses associated with the further turbulence. The Straight inlet receives the least power at all speeds as a base configuration with the least success of running to a desired flow condition. The low-lying linear separation of the curves indicates inlet geometry is affecting the velocity of the whole system. These findings prove that power generation can be greatly improved by an inlet design that is optimized without increasing the operating velocity. In general, Figure 11 indicates that Ring inlet has the best performance at generating the max electrical output by matching flow conditions. Figure 12 shows the impact of air velocity on the thermal to electrical efficiency of the system for Straight inlet, Ring inlet and V-shape inlet configurations. In the case of the lowest velocity of 0.5 m/s, efficiency is very narrow at about 7.2% for the Straight inlet, roughly 9.1% for the Ring inlet and almost 7.8% for the V-shape inlet, indicating poor convection heat transfer and energy recovery at low flow rates. At a velocity of 1.0 m/s, efficiency increases to about 13.1% (Straight), 17.3% (Ring) and 13.6% (V-shape), signifying greater fluidization of the sand bed and better exchange between the heated air and the reactor. At the highest velocity of 1.5 m/s the efficiencies peak at about 16.2% for Straight, 22.1% for Ring and 16.3% for V-shape, indicating higher airflow intensifies heat transfer and electrical generation. This behavior is explained by a higher Reynolds number that decreases thermal boundary layer thickness and increases convective heat flux towards the energy conversion step. The Ring inlet provides the best efficiency at all velocities because its inlet layout is more uniform and entrance losses are low, leading to more energy being converted to electrical supply due to minimum losses. At lower and intermediate velocities the V-shape inlet is marginally more effective than the Straight inlet with greater mixing, but the addition of turbulence holds back its efficiency improvements at higher speeds. The easiest and least efficient inlet of all is the Straight inlet, which is a reference case and performs worse as flow conditioning. As for the increasing separation between the Ring curve and other geometries at higher velocity, they indicate that it was an increasingly important inlet design issue under increased operating conditions. In summary, Figure 12 illustrates that both the airflow rate and the geometry of the inlet significantly impact the efficiency of the system, and that the configuration of the Ring provides the best thermal-to-electrical conversion performance. At fixed air speed and sand load, the pressure drop with temperature setpoint for the Straight, Ring and V-shape inlet geometries can be seen in Figure 13. At the lowest temperature of 30 °C, the pressure drop is about 257 Pa in the Straight inlet, about 205 Pa in the Ring inlet and about 303 Pa in the V-shape inlet, to the extent that the geometric effects are controlling the flow resistance even at moderate thermal condition. Above 60 °C the ΔP slightly increases to approximately 260 Pa (Straight), 208 Pa (Ring), 307 Pa (V) and the resulting increasing of air density and viscosity can be attributed to a small increase in heating factor. At the highest temperature (90 °C) the pressure drop is almost slightly higher at about 263 Pa for Straight, 211 Pa for Ring, and around 310 Pa for V-shape inlet. This relatively weak dependence on temperature, in physical terms, indicates that hydrodynamic losses are mainly a product of inlet geometry, packing resistance and not thermal effects. The Ring inlet always suffers the least pressure drop at all temperatures, indicating its best performance in absorbing the incoming flow evenly and the elimination of

the area of local acceleration. In comparison, the V structure maintains the largest ΔP as a result of an increased turbulence and direct flow through its inclined channels. The Straight inlet is intermediate and gives it a baseline with a moderate resistance. The almost close trend of the curves shows that the relationship between the inlet geometries, in terms of relative ranking, is barely affected when the temperature is increased. This response suggests that fluctuations in temperatures under the experimentally controlled conditions are mainly a temperature parameter but not a loss of aerodynamics. Taken together as shown in Figure 13, whereas heating slightly enhances the pressure drop, the design of the inlet is the primary factor determining the hydrodynamic resistance exhibited in the system. Variation of generated electrical power at temperature setpoint of Straight, Ring and V-shape inlet configurations with consistent flow at the same packing conditions is illustrated in Figure 14. At 30 °C, the electrical discharge is fairly low, approximately 1.28 W of Straight inlet, about 1.60 W of Ring inlet, and approximately 1.38 W of V-shape inlet due to the small heat transfer energy. While increased temperature to 60 °C the power increased significantly to around 1.75 W (Straight), 2.19 W (Ring) and 1.89 W (V-shape), confirming enhanced heat transfer from the warm air to the functional fluid and increased turbine excitation. At the setpoint of the highest 90 °C value, electrical power reaches its maximum values ≈ 2.22 W for Straight, 2.78 W for Ring, and 2.40 W for V-shape, confirming the significant positive influence of temperature on energy recovery. This trend is due to the increase in the enthalpy of the air and temperature gradient resulting in better convective heat transfer, thus increasing the fraction of thermal energy available for conversion. The Ring inlet produces the highest power output even though under the maximum flow distributions at different temperatures are due to its stable flow distribution and lower entrance losses leading to the better extraction of heat from the supplied heat. Second, the V-shape inlet has good mixing, aided through enhanced mixing, but with additional turbulence-induced losses. Most of the electrical power is delivered by the Straight inlet which is a reference case. The proportional response of each geometry to temperature to electrical excitation results indicates that the thermal input directly and vice-versa is converted into electrical output. It is clear to notice how operation temperature has a large effect on power production by increasing it by the power output of each geometrical configuration, and how well the heat input of the inlet was absorbed by the thermal temperature itself.

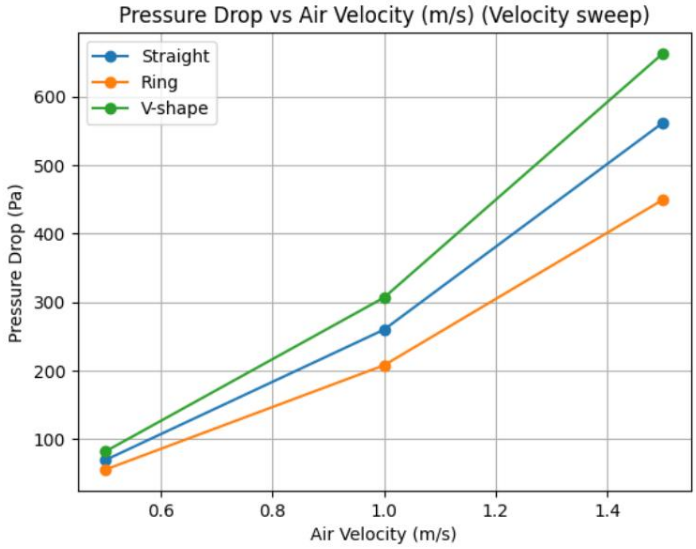

Figure 10. Effect of Air Velocity on Pressure Drop for Different Inlet Geometries

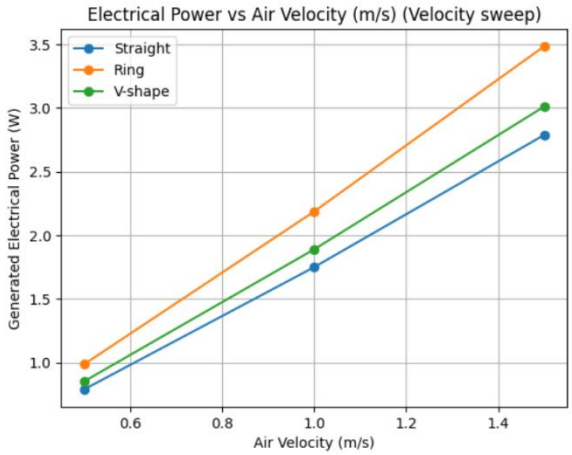

Figure 11. Variation of Generated Electrical Power with Air Velocity for Different Inlet Geometries

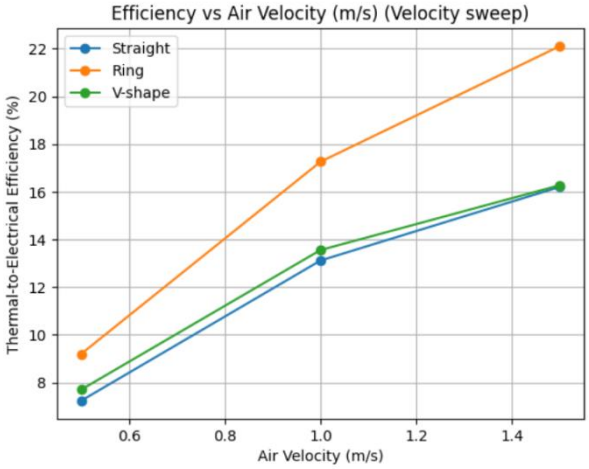

Figure 12. Variation of Thermal-to-Electrical Efficiency with Air Velocity for Different Inlet Geometries

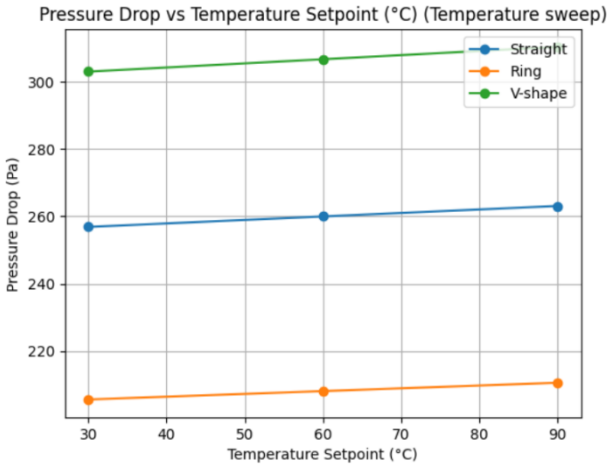

Figure 13. Effect of Temperature Setpoint on Pressure Drop for Different Inlet Geometries

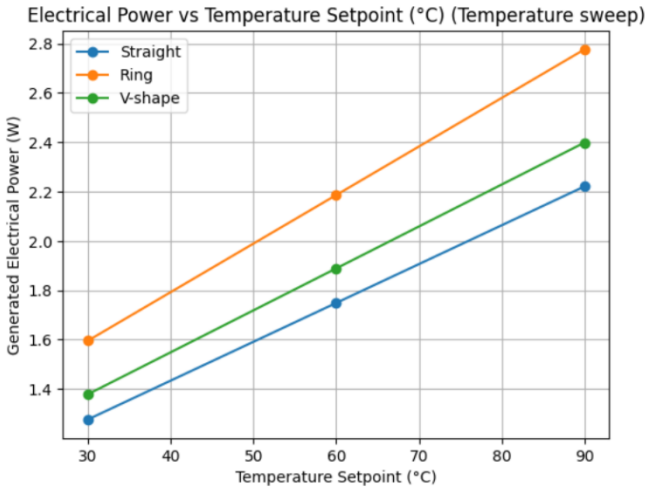

Figure 14. Influence of Temperature Setpoint on Generated Electrical Power for Different Inlet Geometries

Figure 15 shows the effects of temperature setpoint on the thermal-to-electrical efficiency of the system for Straight, Ring and V-shape inlet arrangements at fixed air velocity and sand mass. The maximum efficiency of the design is relatively small at 30 °C, and the efficiency is only about 9.6% at the Straight, approximately 12.6% and 10.0% for the Ring and V-shape inlet, respectively. At higher temperature, when at 60 °C, the efficiency is relatively modest to about 13.1% (Straight), 17.3% (Ring) and 13.6% (V-shape) showing better convective heat transfer and high energy extraction from the heated air stream. A high setpoint of at 90 °C results in maximum efficiencies (~16.6% for Straight, 21.9% for Ring, 17.1% V-shape), which confirms that thermal-to-electrical conversion is strongly promoted at higher inlet temperatures. A significant increase in temperature gradient results in this property, and, mechanically speaking, this results in an increased heat flux and higher enthalpy for generating power from the heated air. Due to its uniform flow distribution and lower entrance losses, the Ring inlet achieves the strongest efficiency throughout all temperatures and thus maximizes the thermal energy provided. The V-shape inlet shows intermediate performance. Because it promotes better mixing, but to some extent it is restrained by turbulence on ground. The smallest efficiency shows up for the straight inlet which takes as its empirical background. The linear increase in efficiency with temperature for all geometries illustrates that thermal input will consistently dominate system function. Furthermore the unbroken shape of the curves indicates that the type and layout of the inlet is still critical, even with the increase in the temperature of the inlet. From the bottom line, Figure 15 shows that the increasing temperature enhances conversion efficiency; Ring inlet has the best thermal to electrical values for the evaluated applications. In Figure 16, we show how sand mass affects the pressure drop throughout the reactor between the Straight, Ring, and V-shape inlet configurations at constant air velocity and temperature. At 100 g, at the smallest sand load, the pressure drop is approximately 237 Pa for the Straight, 189 Pa for the Ring, and ~279 Pa for the V-shape inlet, highlighting for a small packed bed the remarkable flow resistance. With 200 g sand, ΔP increases to roughly 260 Pa (Straight), 208 Pa (Ring), and 307 Pa (V-shape) reflecting the larger solid volume fraction and the reduced space available for airflow. The maximum sand mass of 300 g results in an increase of pressure drop to roughly 284 Pa for Straight, 227 Pa for Ring, and approximately 334 Pa for V-shape inlet, confirming that the denser packing drastically amplifies hydrodynamic loss. Physically, this process corresponds to the enhanced frictional interfacial effect of the air stream with granular medium, but also to the restriction of flow

passages in the bed. The Ring inlet consistently has the lowest pressure drop of any sand mass, as a consequence of the more regular distribution of the flow, and less local jetting at the entrance. On the other hand, the V-shape inlet shows the highest ΔP due to the increasing turbulence due to the divided shape of the inlet flowing through that in addition to it promoting the interaction between surface particles and fluid is also stronger. Once again with the Straight inlet it gets caught between these two extremes where it is a reference configuration for moderate resistance. The almost linear scaling up of ΔP with sand mass per all geometries confirms the proportional relationship between solid loading and flow resistance in the simulated range. These results confirm that the concentration of particles is one of the parameters that is essential to control pressure dissipation in the reactor. This demonstrates the significance of optimizing both inlet geometry and sand mass at both ends — effective fluidization versus excessive pressure drop (Figure 16). Dynamic electrical power response with sand mass for Straight, Ring, and V-shape inlet configuration with consistent air velocity and temperature: Figure 17 At a minimum sand load of 100 g, the electrical power reaches about: 1.47 W for the Straight inlet, ∼1.83 W for the Ring inlet, approximately 1.58 W for the V-shape inlet showing a restricted heat transfer and momentum exchange given the sparse distribution of particles. At the 200 g sand load, the power level increases approximately 1.75 W (Straight), 2.18 W (Ring) and 1.89 W (V-shape), indicating that the moderate particle concentration makes for better fluid–solid interaction and better thermal mixing and energy extraction. For the highest sand mass of 300 g, however, the electrical power comes down to a value of about 1.60 W for Straight, 2.00 W for Ring and approximately 1.73 W for V-shape inlet, indicating that there has been the emergence of excessive flow resistance and partial bed choking. And in the natural physics, this non-monotonic tendency corresponds to a competition between a better heat transfer condition on intermediate sand loading, and a higher rate of pressure drop at high packing densities. The Ring inlet delivers the highest power in all sand masses always due to its uniform distribution of the flow and smaller entrance losses. V-shape inlet, on the other hand, comes next with better mixing but the constraint of an excessive turbulence. It should be noted that the Straight inlet is again the one with the lowest electrical output and this is the baseline configuration. The existence of optimum around 200 g for all geometries suggests that an ideal particle load will maximise the energy output. Findings show that concentration of the particles have to be fine-tuned to not reduce energy generation because of high hydrodynamic resistance. In conclusion, as seen through Figure 17, moderate sand mass offers the biggest compromise between enhancing heat transfer and pressure drop penalty with Ring inlet producing the best performance. At fixed air velocity and temperature, the influence of sand mass on the thermal-to-electrical efficiency of the system for the Straight, Ring, and V-shape inlet configurations is shown in figure 18. With 100 g sand loading the efficiency is approximately 11.3 % for the Straight inlet, 14.8 % for the Ring inlet, and close to 11.7 % for V-shape inlet, which reflects the insufficient potential for heat transfer enhancement and lower heat transfer capacity resulting from relatively dilute particle bed. Once 200 g sand mass is introduced, the efficiency reaches its peak at 13.1% (Straight), 17.2% (Ring), and 13.5% (V-shape), indicating intermediate particle content confers an ideal operating conditions for convective heat exchange and energy recovery. However, at the high sand mass of 300 g, the efficiency is around 11.8% for Straight, 15.5% for Ring, and ∼12.1% for V-shape inlet which demonstrates that too much packing decreases effective flow permeability and thermal efficiency. In terms of the physics, this non-monotonic property is due to the battle between the higher surface area and better mixing at moderate sand loading, and pressure losses and decrease in the void fraction at high particle contents. Due to uniform flow and reduced entrance losses, the Ring inlet always performs at the best level of efficiency for all sand masses, and hence more

effective thermal energy was utilized. The V-shape inlet represents an intermediate performance, having improved blending capability but still limited by additional turbulence induced losses. The Straight inlet is again providing the lowest efficiency and becomes the baseline case. With all geometries having a clear optimum of about 200 g, we see that there is indeed a solid loading condition that can maximize the conversion efficiency. These findings highlight that particle mass is an important design consideration in thermo-fluid energy systems. In general, as depicted in Figure 18, moderate sand mass has the greatest trade-off between enhanced heat transfer and hydrodynamic negative impacts, where the Ring inlet has the best thermal-to-electrical performance. We observe that the Straight inlet achieves the highest pressure drop of 260 Pa, the Ring induces a pressure drop of 208 Pa when the air velocity is 1.0 m/s, at the temperature 60 °C and the sand mass is 200 g, as compared to the Straight, Ring, and V configurations (F=10). In contrast, V-shaped inlet gives the highest pressure drop with a value of about 307 Pa. Physically, this behavior also reflects the differing entrance flow features posed by each geometry. The Ring inlet, as an inlet, achieves a lower ΔP, by spreading the load (influence air in the reactor) around the reactor circumference, such that the acceleration, jet impingement and recirculation zones are little regionally localized. The Straight inlet induces a straight axis inlet that yields moderate resistance, which is useful as a standard configuration. Whereas on the contrary, the V-shape inlet causes the flow to split and to change direction sharply, and hence the turbulence increase and also the frictional loss increase which result in the maximum pressure penalty. This separation of the three bars indicates the most important effect of inlet design on the hydrodynamic behaviour although all other parameters of operation are fixed. These measurements show that geometry can change the pressure drop by close to 100 Pa in the inlet box between Ring and V shape. Such divergence directly results in different pumping power requirements for real-world systems. From a hydraulic perspective, therefore, for the Ring inlet flow entry is best, while the V-shape inlet enters with largest energy cost. In conclusion, Figure 19 proves that the inlet design approach is crucial in order to reduce hydraulic pressure losses, while still maximizing the energy efficiency of the thermo-fluid energy conversion system.

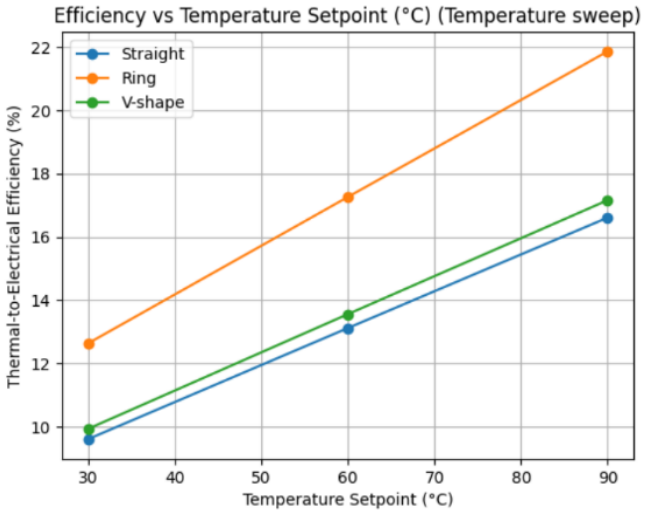

Figure 15. Effect of Temperature Setpoint on Thermal-to-Electrical Efficiency for Different Inlet Geometries

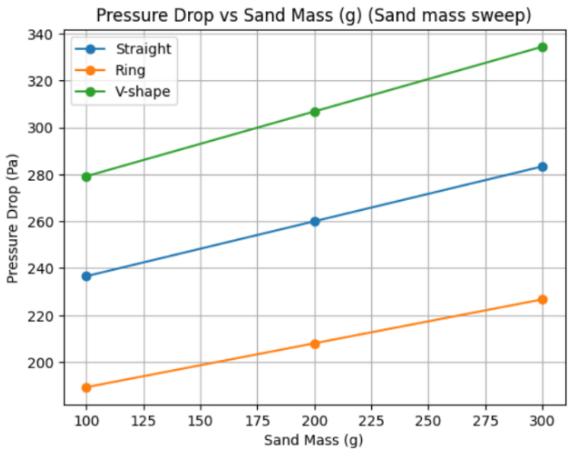

Figure 16. Influence of Sand Mass on Pressure Drop for Different Inlet Geometries

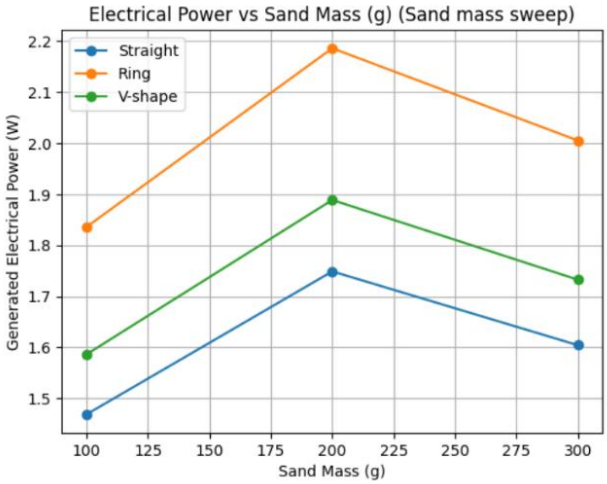

Figure 17. Effect of Sand Mass on Generated Electrical Power for Different Inlet Geometries

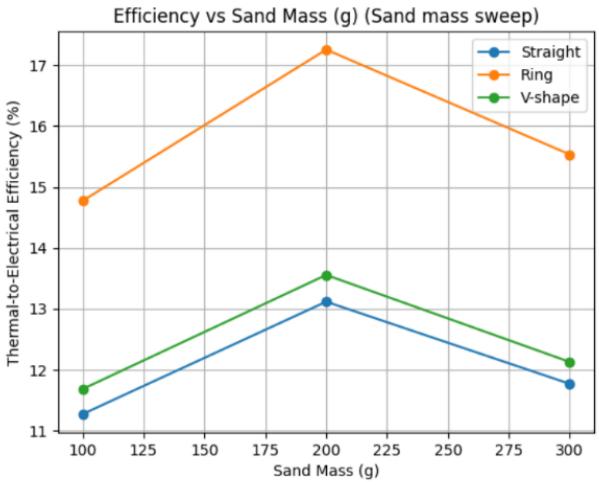

Figure 18. Effect of Sand Mass on Thermal-to-Electrical Efficiency for Different Inlet Geometries

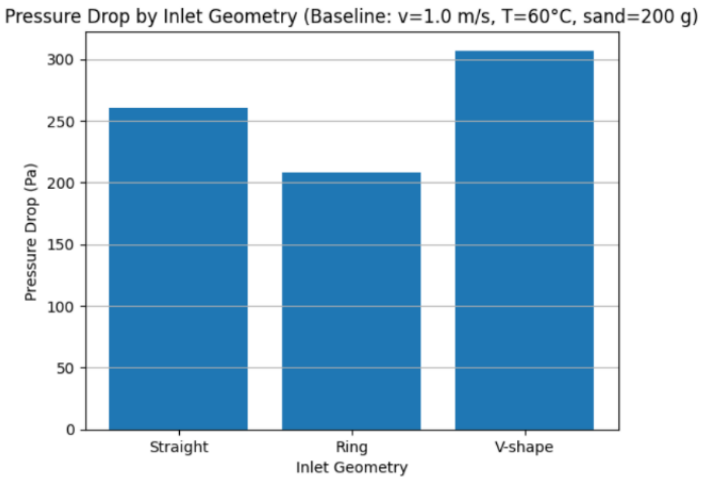

Figure 19. Comparison of Pressure Drop for Different Inlet Geometries at Baseline Operating Conditions

Electricity produced by the Straight, Ring, and V configuration are estimated given the air velocity 1.0 m/s, temperature 60 °C and sand mass 200 g in Figure 20, where the Straight inlet generates about 1.75 W, and the Ring inlet the maximum electrical power of approximately 2.20 W, while the V-shape inlet gives an intermediate value of approximately 1.90 W. Physically these differences can be summarized as the manner that each inlet conditions the incoming flow and determines the heat and momentum transfer in the reactor. The Ring inlet contributes to power generation by spreading the air in an even distribution of the column, so that the sand becomes more uniform and is able to receive better thermal exchange and more fraction of the supplied thermal energy can be directly transformed into efficient electrical power. The Straight injection has an axial jet that does not mix as uniformly, thus a smaller energy recovery. The V-shape inlet enhances mixing compared to the Straight case because of flow splitting but its increasing turbulence and entrance losses reduce the electrical output vis-à-vis the Ring configuration. The fact that the Ring and Straight inlets are a similar value that is about 0.45 W apart indicates how much is influenced by the inlet configuration of the inlet when the working conditions are the same. The findings show that inlet shape can directly affect the produced electrical power by more than 25% in this system. From an energy conversion standpoint, the Ring inlet provides a more acceptable trade-off between flow delivery and hydraulic losses. By and large, the data from Figure 20 shows that optimizing the inlet geometry as such is a valuable procedure to obtain maximum electrical power in thermo-fluid energy conversion systems. In Figure 21, we visualize a complete trade-off map showing the magnitude of the pressure drop and the thermal-to-electrical efficiency ratio of generated electrical power at different operating conditions and inlet geometries. The system generates weak electricity at low pressure of not more than 100 Pa around 0.5–1.2 W, yielding few efficiencies, of 4–8%, which denotes weak fluidization and lack of heat transfer. The electrical power increases at intermediate levels of about 200–400 Pa and the efficiency increases to about 10–18%, the result being increased mixing of the sand bed and stronger convective heat exchange. In the upper pressure-drop region, located between ~400 and ~700 Pa, the electrical output is up to ~3.5–4.5 W and the maximum efficiency is ~25–28%, which indicates high effective thermal energy recovery and intense fluidization. Physically this demonstrates the tight coupling between hydrodynamic losses and energy recovery: greater ΔP means greater momentum and heat transfer of airflow, raising power production but also higher pumping costs. The color gradient demonstrates, quite explicitly, that the highest point of the optimum

op-top are found in the upper-right of the plot where the pressure drop and power are high. In contrast, in the lower-left region, you see low efficiency situations with low flow and lower amount of power exchange. The wide spread of points reflects the overall effect of the inlet geometry, air velocity, temperature and sand weight on system performance. Many of the mid-range ΔP's have relatively high power and moderate efficiency at various points, indicating prospective operating windows where the energy produced and the hydraulic cost is compromised. So this map gives a useful tool to extract operational regimes at optimal conditions. In a nutshell, Figure 21 shows that generally to obtain maximum electrical power higher pressure losses are needed and that it is crucial to optimise the inlet and operating condition to obtain an effective trade off of the efficiency plus the driving demands. For a Straight inlet configuration, thermal to electrical efficiency shown in Figure 22, in relation to air velocity (0.5–1.5 m/s) and temperature setpoint (30–90 °C) at a fixed sand mass of 200 g, is clearly two-dimensional, and at the lowest efficiency value (0.5 m/s and 30 °C), which is close to 5–6 %, the degree of fluidization is low as is the thermal forcing. Higher performance results for either parameter; for example, 1.0 m/s and 60 °C results in an efficiency higher than 12–13% signifying more convective heat transfer and better particle–fluid interaction. The greatest efficiencies, > 20%, are at the combined high-velocity and high-temperature condition (1.5 m/s and 90 °C), in which energy extraction is maximized by increased airflow and thermal gradients. Physically, the color progression from dark blue to yellow illustrates how increasing Reynolds number and temperature difference jointly reduce thermal boundary layers and intensify heat exchange within the packed bed. The nearly monotonic increase along both axes confirms that airflow rate and thermal input act synergistically to improve conversion efficiency. However, the gradient is steeper in the velocity direction, suggesting that hydrodynamic enhancement plays a slightly more dominant role than temperature alone for the Straight inlet. The intermediate region (around 1.0 m/s and 60 °C) represents a practical operating window where moderate efficiency is achieved without extreme pressure losses. Overall, Figure 22 demonstrates that the Straight inlet benefits significantly from simultaneous increases in air velocity and temperature, although its absolute efficiency remains lower than that of optimized geometries. This heatmap provides a compact visualization of the coupled thermo-fluid effects governing system performance and helps identify favorable operating regimes for this baseline configuration. Thermal-to-electrical efficiency distribution shows that air velocity at an observed temperature (0.5 to 1.5 m/s) and temperature set point (30 to 90 °C) for a constant sand mass of 200 g for the Ring inlet configuration is very low at the lowest operating condition (0.5 m/s and 30 °C), about 7 to 8%, indicating very weak fluidization and limited thermal driving potential. With an increase in velocity or temperature, efficiency dramatically improves; e.g., at 1.0 m/s and 60 °C, it becomes 17–18%, indicating enhanced convective heat transfer since the annular inlet contributes to more homogeneous particle motion. The highest efficiency values (27–28%) are reached during the combined high-velocity and high-temperature conditions which together result in substantially increased airflow and increased thermal gradients to maximize power generation. Physically, this better performance is due to the circular pattern of air being supplied to the Ring inlet and distributed evenly around the top of the reactor, minimizing localized jets, leading to smooth fluidization of the sand bed. The smooth color transition from dark blue to bright yellow confirms the nearly monotonic increase in efficiency along both axes, indicating the synergistic effect of hydrodynamic and thermal intensification. The Ring heatmap compared with the Straight inlet heatmap attains much better efficiency across all operating points, indicating the increased flow conditioning capability of the Ring configuration. Figure 24 presents the thermal-to-electrical efficiency map for the V-shape inlet configuration over air velocities of 0.5–1.5 m/s and temperature setpoints of 30–90 °C at a constant sand mass

of 200 g. At the lowest operating condition (0.5 m/s and 30 °C), the efficiency is limited to about 5–6%, reflecting weak fluidization and insufficient thermal driving force. Increasing either air velocity or temperature results in a clear enhancement in efficiency; for example, at 1.0 m/s and 60 °C the efficiency reaches approximately 12–13%, indicating stronger mixing and improved heat transfer induced by the inclined inlet channels. The highest efficiency, close to 20–21%, is observed at the combined high-velocity and high-temperature condition (1.5 m/s and 90 °C), where intensified airflow and elevated thermal gradients maximize energy extraction. Physically, the V-shape inlet promotes flow splitting and increased turbulence, which enhances particle agitation and convective heat exchange, but also introduces additional hydrodynamic losses compared to the Ring geometry. The progressive color transition from dark blue to yellow demonstrates the synergistic effect of velocity and temperature on system performance. Compared with the Straight inlet, the V-shape configuration achieves moderately higher efficiencies due to improved mixing, while remaining consistently below the Ring inlet because of its larger pressure penalties. The intermediate operating region around 1.0 m/s and 60 °C provides a balanced compromise between efficiency gain and flow resistance. Overall, Figure 24 confirms that the V-shape inlet benefits substantially from increased airflow and temperature, yet its performance is constrained by enhanced turbulence. These results emphasize that while aggressive inlet designs can improve heat transfer, their associated pressure losses must be carefully managed to achieve optimal thermo-fluid energy conversion.

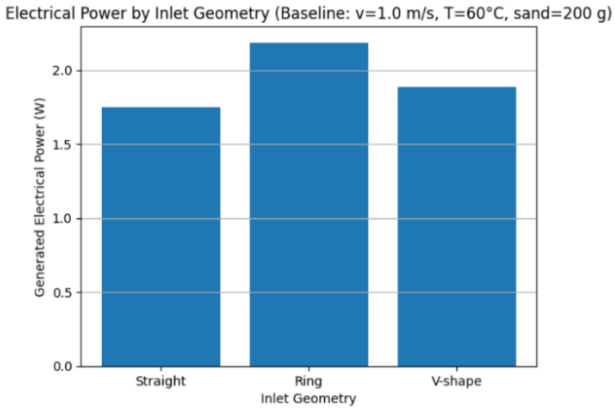

Figure 20. Comparison of Generated Electrical Power for Different Inlet Geometries at Baseline Operating Conditions

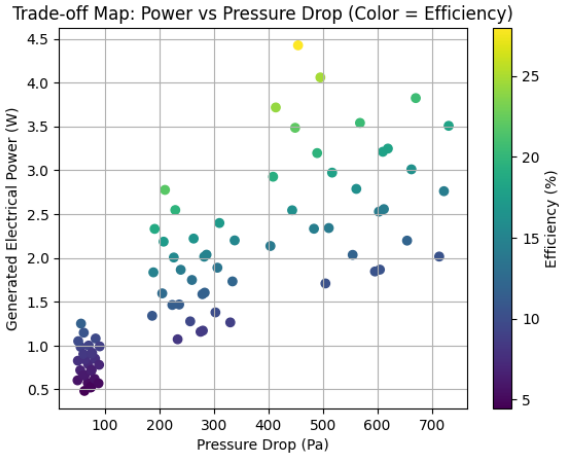

Figure 21. Trade-off Map between Generated Electrical Power and Pressure Drop with Efficiency as Color Indicator

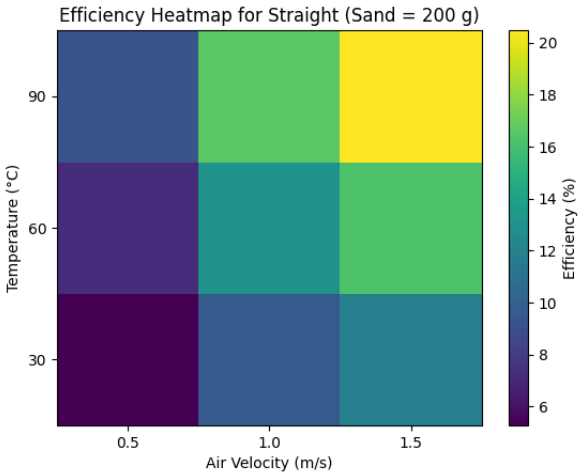

Figure 22. Efficiency Heatmap for Straight Inlet as a Function of Air Velocity and Temperature (Sand Mass = 200 g)

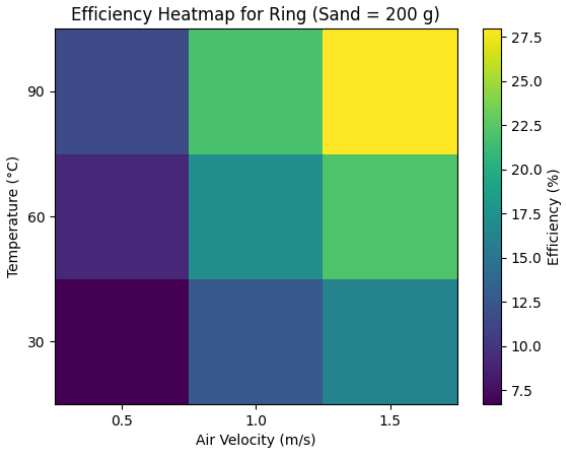

Figure 23. Efficiency Heatmap for Ring Inlet as a Function of Air Velocity and Temperature (Sand Mass = 200 g)

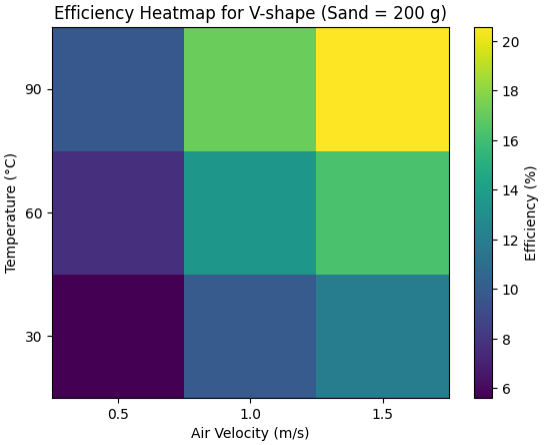

Figure 24. Efficiency Heatmap for V-Shape Inlet as a Function of Air Velocity and Temperature (Sand Mass = 200 g)

The thermal-to-electrical efficiency of the straight inlet configuration is calculated from air velocity (0.5-1.5 m/s) and sand mass (100-300 g), at a fixed temperature of 60 °C, and the worst at 0.5 m/s is found to reach about 6-7% at 100 g, around 7-8% at 200 g, or around 7% at 300 g, which all imply not enough fluidization and less heat transfer when the aerodynamic force is weak. At 1.0 m/s the efficiency significantly increases to around 11–12% for 100 g, about 13–14% for 200 g, and roughly 12% for 300 g, indicating that particle motion and convection heat exchange are better. The maximum efficiency at 1.5 m/s has been observed, being

around 14 to 15% at 100 g, peaking at approximately 16% for 200 g and reducing to around 14 to 15% for 300 g in this case visually. The pattern that is being exhibited further illustrates that with increasing airflow the heat transfer improves by enhanced fluidization of the sand, an intermediate sand mass offers the right ratio of surface area and flow permeability. Its central peak at 200 g demonstrates that there is an optimum for the particle loading at the Straight inlet, that the more air is crammed, the higher resistance generated and that further efficiency is no longer achieved. The color patterns also show that in the tested areas, for airflow compared to the mass of the sand, it has a significant impact compared to the other mass value for performance. In essence, Figure 25 stresses that for the Straight geometry, high air velocity together with moderate sand loading exhibits the greatest efficiency. However hydrodynamic and particle concentration is dynamically coupled with one another and determines the properties of high power transfer performances. Thermal-to-electrical efficiency of the Ring inlet configuration with air velocity (0.5–1.5 m/s) and sand mass (100–300 g) is depicted in Figure 26 under constant temperature of 60 °C. The lowest velocity of 0.5 m/s has relatively small efficiencies, which then increase to around 8% at 100 g, nearly 9–10% at 200 g, and then stabilize at around 8–9% at 300 g, showing poor fluidization and a lack of convective heat transfer. When increasing the velocity to 1.0 m/s, there is a considerable increase in efficiencies to roughly 14–15% at 100 g, about 17–18% at 200 g and nearly 15% at 300 g, reflecting better mixing of particles, brought about by the annular air distribution. Efficiency was highest at 1.5 m/s, reaching approximately 19–20% at 100 g, peaking at the range of ∼22% for 200 g and slightly declining to ∼20% at 300 g, mainly due to the continuous circular airflow to the Ring inlet, which facilitates sand agitation and heat extraction and reduces localized stagnation zones. The clear peak at 200 g confirms a good sand loading conditions in which both surface area availability and flow permeation are harmoniously balanced. Beyond this point, additional sand causes a greater resistance to flow and fewer further advantages. The color gradients show that air velocity has more than a strong influence on efficiency in the system, and the amount of sand mass plays an indirect as significant part. Generally, and after the investigation of Figure 26, the findings indicate that the Ring inlet consistently outperforms the straight geometry at exactly the same conditions, showing its best performance at high airflow/s at moderate sand mass. These observations further substantiate that annular inlet distributions can lead to optimal thermo-fluid energy conversion. Figure 27 demonstrates the thermal-to-electrical efficiency variation for V-shape inlet, having varying air velocity (0.5–1.5 m/s) and sand mass (100–300 g), at the fixed temperature of 60 °C. The efficiencies are small at the lowest velocity of 0.5 m/s with efficiencies up to 6–7% at 100 g, slight enhancement to 8–9% at 200 g, and remaining around 7–8% at 300 g, showing the poor particle mobilization and the weak heat transfer during low aerodynamic forcing. As the velocity increases to 1.0 m/s, there is an obvious improvement in efficiency, reaching about 11–12% at 100 g, 14% at 200 g and close to 12–13% at 300 g indicating increase in turbulence and better mixing due to the inclined inlet channels. At peak efficacy (1.5 m/s), efficiency attained approximately 15% at 100 g, 16–17% at 200 g and then slightly decreasing to roughly 15% at 300 g, thus it is the V-shape inlet contributes to enhancing flow impingement with an increase in sand agitation, and convective heat flow, whereas with excessive sand loading increasing resistance and consequently the net gain. The prominent peak at 200 g once more reflects an ideal particle mass, wherein surface area and permeability are balanced. The colour gradients indicate that air velocity is the most significant control parameter and there is a secondary modulation of sand mass. When comparing with the Straight inlet the V-shape possesses better efficiencies because of more intensive mixing, but does not reach as high and is consistently below the Ring inlet due to extra pressure losses. The V-shape provides the best benefit when there is high airflow combined with moderate sand mass, but its aggressive flow redirection weakens performance, as shown in Figure 27. A three-dimensional surface with the influence of

air velocity (0.5–1.5 m/s) and temperature setpoint (30–90 °C) over the thermal-to-electrical efficiency at a fixed sand mass of 200 g is shown in Figure 28, which clearly shows a monotonic increase in efficiency for both axes, illustrating the synergistic role of hydrodynamic intensification and thermal driving force. It is limited to operating at 0.5 m/s and 30 °C at its minimum efficiency of approximately 7–8%, which indicates low convection strength and lack of particle agitation. Increased velocity up to 1.0 m/s at this temperature raises the efficiency to approx. 12–13%. Further increasing the temperature to 60 °C increases the efficiency to ca. 17–18%, indicating intense susceptibility of the system to thermal input. The best efficiency, which approaches 27–28%, is obtained by a high combination of velocity and temperature (1.5 m/s and 90 °C), and the high airflow uniformly distributed through the annular inlet leads to the highest possibility of sand fluidization and convective heat transfer. Smooth curves of the surface indicate a near-linear response in the investigated interval, that is, no abrupt local optimum results and thus a stable system behavior. The direction of air interaction that results in enhanced interfacial heat transfer coefficients increased with high air velocities whereas the thermoelectric driving gradient got larger as temperatures increased. The trajectory along the incline to the high velocity/high temperature corner emphasizes that neither parameter alone is enough to achieve the optimum performance and that energy conversion occurs by coupling the two. It is demonstrated in Figure 28 in full that the Ring inlet is an efficient platform for the extraction of thermo-fluid energy, with a peak working state under high airflow and temperature together. A significant monotonic gain in efficiency is seen when air velocity increases as it goes up from 0.5 to 1.5 m/s. At the lowest velocity of 0.5 m/s, the average efficiency is approximately 7–8%, resulting in weak fluidization, very little turbulence and reduced convective heat transfer between the heated air, sand particles, and thermoelectric module. When increasing the velocity to 1.0 m/s, a great improvement occurs; the average efficiency is about 13–14%, showing faster particle agitation and better heat transfer due to higher Reynolds numbers. When the velocity increases to 1.5 m/s, the increase in the efficiency is still higher (approximately 16–17%), hence airflow rate remains the predominant control variable in the system. Theoretically, the increased velocity increases mixing strength, decreases thermal boundary-layer thickness, and improves temperature uniformity and thus electrical output. The nearly linear trend indicates that, within the range studied, aerodynamic improvement is the main advantage over additional pressure losses. In general, it is confirmed in Figure 29 that air velocity has the greatest effect on individual performance showing that proper flow driving is very important in thermo-fluid energy conversion systems.

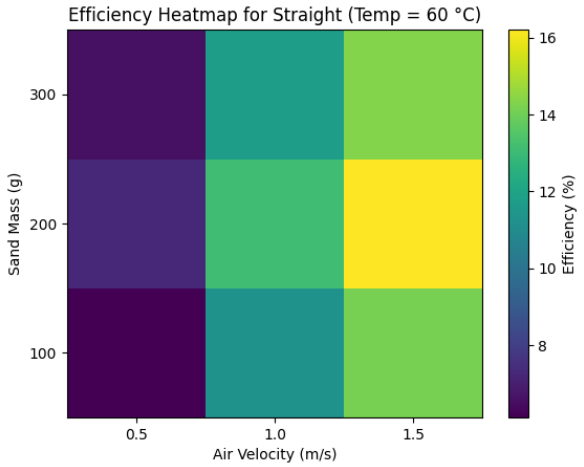

Figure 25. Efficiency Heatmap for Straight Inlet as a Function of Air Velocity and Sand Mass (Temperature = 60 °C)

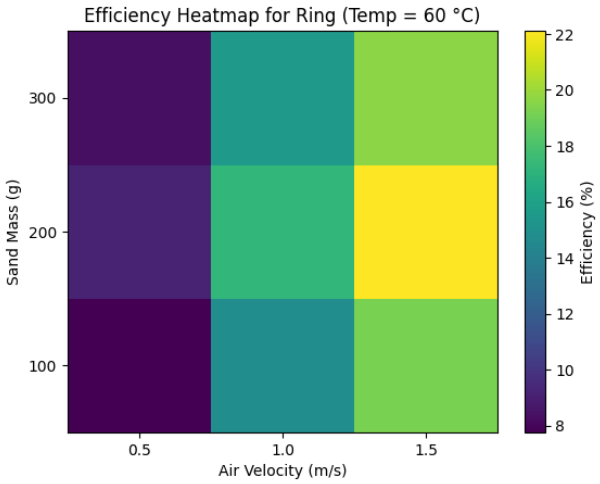

Figure 26. Efficiency Heatmap for Ring Inlet as a Function of Air Velocity and Sand Mass (Temperature = 60 °C)

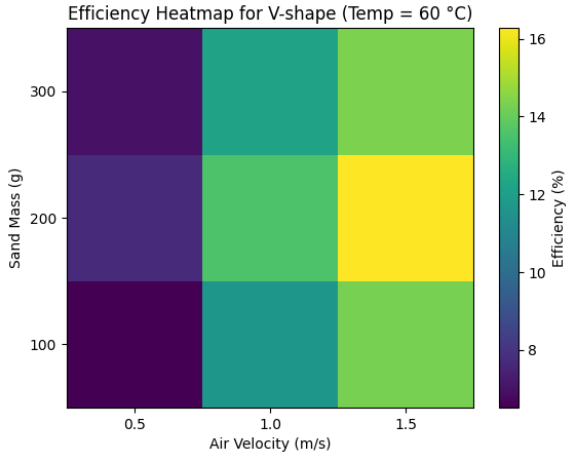

Figure 27. Efficiency Heatmap for V-Shape Inlet as a Function of Air Velocity and Sand Mass (Temperature = 60 °C)

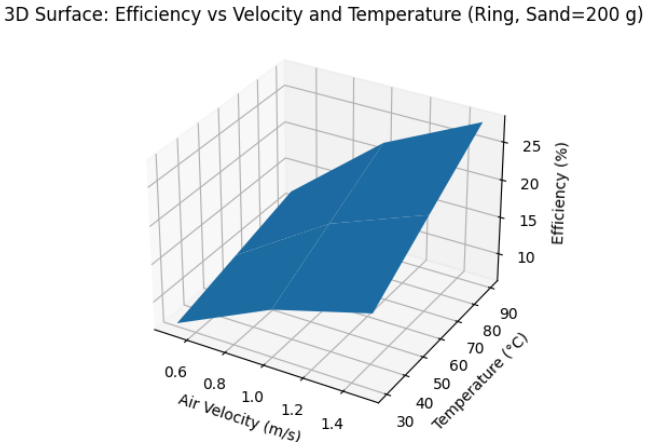

Figure 28. Three-Dimensional Efficiency Surface for Ring Inlet as a Function of Air Velocity and Temperature (Sand Mass = 200 g)

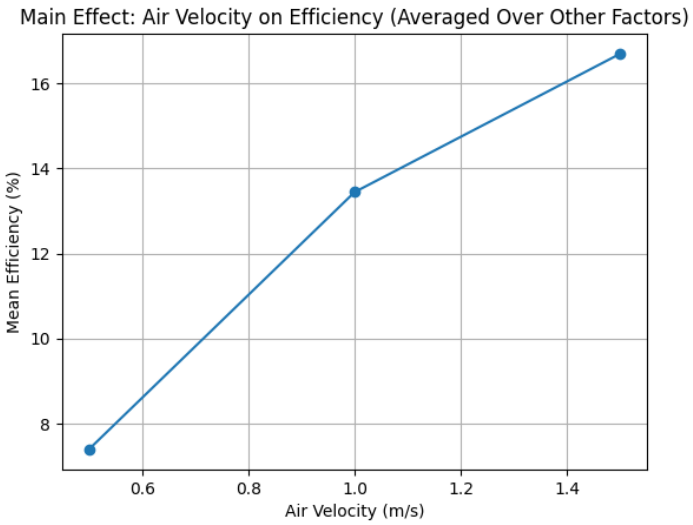

Figure 29. Main Effect of Air Velocity on Thermal-to-Electrical Efficiency (Averaged over Temperature, Sand Mass, and Inlet Geometry)

The mean thermal-to-electrical efficiency (Measurable Efficiency) indicates the impact of temperature setpoint on the mean and the mean averaged from air velocities, sand mass and inlet geometries (see Fig 30). A clear upward trend is clearly noticeable in the range of 30 and 90 °C, and an average efficiency is about 9% to 10%, indicating that the thermoelectric driving force is limited only due to a small heat gradient across the Peltier module. The mean efficiency increases to approximately 12–13% when temperature rises to 60 °C due to improved heat flux and stronger interaction between heat storage source and the energy conversion unit. At an elevated temperature of 90 °C, the efficiency is almost 16%, showing that thermal input is a major impact factor on the enhancement of electrical output. Moreover, the increasing temperature amplifies the thermal potential available at each point of transpiration, increases the temperature variation on the thermal device, increases the transfer of convective heat from the material to the sand bed, and increases the conversion efficiency as thermal source increases from that temperature. The nearly continuous response indicates that the system operates in a stable manner under the condition that is tested with no indication of a thermal saturation. Although slightly weaker in magnitude than the air-velocity main effect, the temperature effect is still very significant. As a whole, we conclude that the performance-enhancing methods of increasing the thermal setpoint require that material limits and structural stability are addressed.

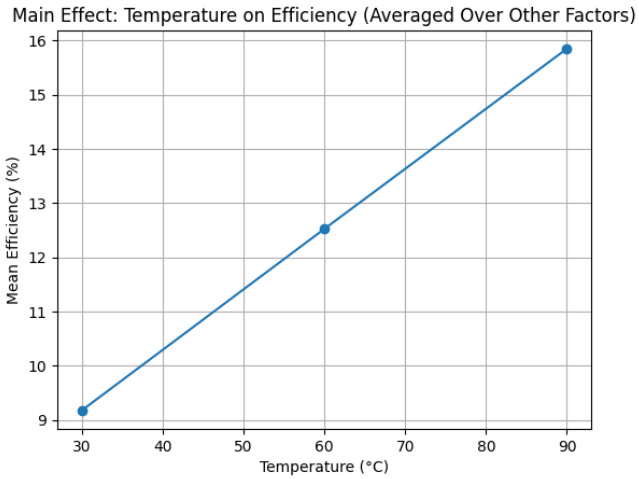

Figure 30. Main Effect of Temperature on Thermal-to-Electrical Efficiency (Averaged over Air Velocity, Sand Mass, and Inlet Geometry)

Fig. 31 shows the most significant contribution of sand mass on the mean thermal-to-electrical efficiency, as the average of such findings among all air velocities, temperatures and inlet geometries. Sand mass, in contrast to air velocity and temperature, has non-monotonic behaviour with a distinct optimum. The mean efficiency is around 11.7–11.8% at 100 g, which indicates that part of the particle inventory cannot be used to provide sufficient thermal storage and interfacial heat transfer area. When sand mass is increased to 200 g, mean efficiency values increase to approximately 13.5–13.6% with a maximum value and indicating an optimum trade-off between available heat capacity, particle surface area and flow permeability. When sand mass is further increased to 300 g, the efficiency declines to ~12.2% as it causes increase in flow resistance, decrease in porosity and partial suppression of effective fluidization. Moderate loading improves thermal buffering and enables uniform heating, while excessive loading causes pressure drop and prevents convective circulation. The highest trend is supported that particle concentration is a secondary, but relevant factor in the system performance, mediating the heat transfer increase efficiency to hydrodynamic impact drawbacks. Moreso than the monotonic effects of air velocity and temperature that seem to prevail for ideal conditions, sand mass mainly determines whether an operating optimum is possible rather than continuous improvement. For the present configuration, approximately 200 g of sand is the optimal case for energy conversion overall in Figure 31, signifying that the bed loading is critical in the thermofluid systems.

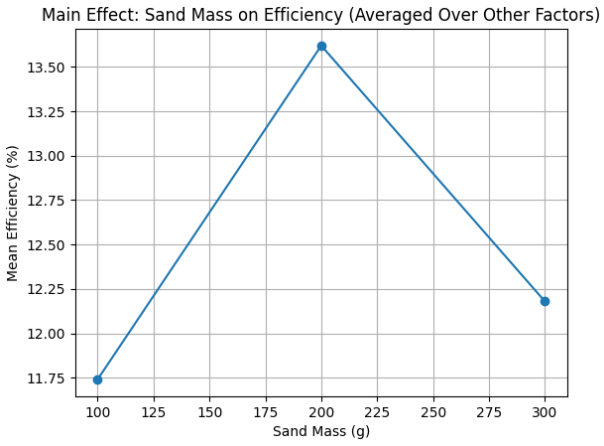

Figure 31. Main Effect of Sand Mass on Thermal-to-Electrical Efficiency (Averaged over Air Velocity, Temperature, and Inlet Geometry)

Thus the results are combined for all air velocities, temperature setpoints, sand mass. The Ring inlet yields inlet efficiencies comparable to those of the Inlet ring and the V-shaped inlet. The mean efficiency of air jet inlet lies between approximately 14.8 percent and 15 percent. The better performance of the Ring geometry is also explained by its circumferential air distribution, which promotes the uniform fluidization of the sand bed, the absence of localized jets, and the greater convective heat transfer to the thermoelectric module. In contrast, the Straight inlet induces a greater concentration of a core flow that results in less homogeneous particle motion and less effective heat exchange. The V-shape inlet induces turbulence and mixing through flow splitting; this method is more effective when compared with the Straight case, but also results in greater pressure loss and restricts its overall efficiency. The clear space of the Ring inlet and the other two geometries show that inlet type has a major impact on system behavior but secondary to air and temperature. In general, as shown in Figure 32, optimized inlet geometry [specifically the Ring configuration] presents the measurable advantage in thermo-fluid energy conversion by balancing the increased mixing and moderate hydrodynamic resistance.

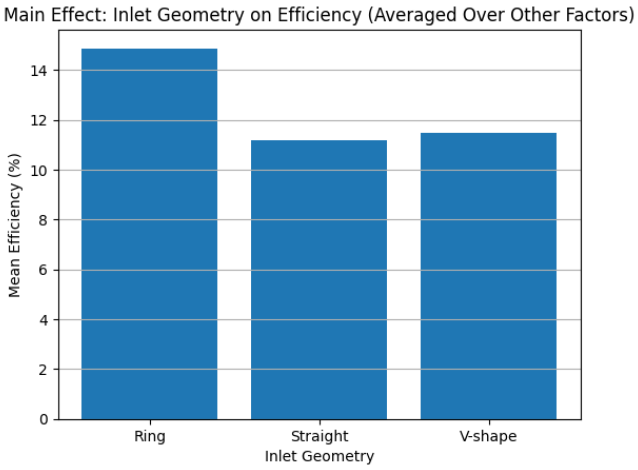

Figure 32. Main Effect of Inlet Geometry on Thermal-to-Electrical Efficiency (Averaged over Air Velocity, Temperature, and Sand Mass)

For these three inlet geometries for identical operating conditions, a qualitative visualization of the sand-bed hydrodynamics within the acrylic column is shown in Figure 33. Concerning the Straight inlet, the airflow produces a predominant central jet which produces a narrow upward channel with a relatively static region near the walls, revealing non-uniform fluidization and no lateral mixing. On the contrary, the Ring inlet creates a more uniform motion of particles, resulting in the sand grains being lifted more homogeneously along the cross section, indicating increased air circulation and reduced jet effect. These more homogeneous effects of the air distribution in the flow can account for higher efficiency results reported before. The V-shaped inlet displays apparent flow splitting, generating inclined jets that amplify local turbulence and particle agitation but also introduces asymmetric circulation and localized high-shear areas. So, the V-shape provides stronger mixing than the Straight inlet in terms of physical performance, although still showing less uniformity than the arrangement on the Ring configuration due to directional impingement of the flow. In the Ring case, the outward bulge and suspension of particles are

similar, confirming better bed activation and efficiency in exploiting the sand volume. The Straight inlet shows only a fraction of channeling, and the V-shape has more aggressive but less uniform spread of agitation. These visual profiles are perfectly in harmony with quantitative trends in pressure drop and operating efficiencies, in which Ring inlet got the best tradeoff between mixing enhancement and hydrodynamic losses. In general, Figure 33 shows how inlet configuration is directly proportional to particle kinetics, flow uniformity and thermo-fluid energy conversion performance.

Figure 33. Visual Comparison of Sand Fluidization Patterns for Straight, Ring, and V-Shape Inlets (Airflow from Bottom to Top)

While previous research explored thermo-fluid enhancement and energy-based applications across engineering systems, it was largely performed on a spectrum of individual performance without an integrated electrical recovery. Abdelmagied (2024) & Rahman (2024a, 2024b) investigated the thermo-fluid profiles of modified heat exchangers for twisted tubes and perforated baffles to demonstrate enhanced heat transfer without coupling to energy conversion devices. Similarly, Acharya et al. (2025) and Rostami and Ahmadi (2025) analyzed turbulence promoters and pipe geometries focused on flow structure and exergy destruction rather than direct electrical power generation. Abdelrehim et al. (2024) and Alrashidi et al. (2025) improved wick absorbers and hydrogel cooling systems in solar systems; however, granular media and inlet-flow control were not included in these studies. Bianco et al. (2023) and Shimada et al. (2024) used phase-change and porous structures to improve thermal transport; however, electrical harvesting techniques were not tested empirically. The thermoacoustic and waste-heat recovery systems were modeled by Baccoli et al. (2025), Di Meglio and Massarotti (2022) and Persico et al. (2024), with a focus on numerical methods. In contrast, the present work combines sand fluidization, controlled inlet geometries, and thermoelectric generation in one single, small framework experimentally. Previous research considered the inlet design a secondary issue, while this research finds that optimized Ring inlet distribution increases electrical power by more than 25%, with peak efficiency at approximately 27–28% for 1.5 m/s and 90 °C, and lower pressure drop compared with Straight and V-shape configurations. In addition, the determination of an appropriate sand mass (200 g) offers valuable guidance on how to achieve a balance of thermal storage and hydrodynamic resistance that has not been studied in previous studies on thermo-fluids. As such, this study extends the previous literature by providing a fully coupled experimental investigation of airflow dynamics, granular response, heat transfer, and electrical energy harvesting, which defines the inlet geometry as a key design parameter for compact thermo-fluid energy conversion systems.

4. Conclusions

Data analysis has shown that inlet shape, velocity of airflow, temperature setpoint, and

mass of sand collectively influence thermo-fluid properties and energy conversion ability of the new sand-based reactor. Among the tested designs, the Ring inlet achieved the best overall performance as it provided the highest electrical power (up to ~3.5 W at 1.5 m/s), maximum thermal-to-electrical efficiency (~ 27–28%) with combined high airflow (1.5 m/s) and high temperature (90 °C), as well as the lowest pressure drop as compared to the Straight and V-shape inlets (e.g., ~450 Pa for Ring versus ~560 Pa for Straight and ~660 Pa for V-shape). Despite the moderate operating conditions of 1.0 m/s, 60 °C, 200 g sand, Ring inlet still beat the other inlets in the mean (2.2 W, efficiency close to 17–18%), while Straight and V-shape inlets produced ~1.75 W and ~1.9 W, respectively, at lower efficiencies. Air velocity had the strongest monotonic effect upon the performance, elevating the average efficiency from about 7–8% at 0.5 m/s to 16–17% at 1.5 m/s as a result of the exaggerated fluidization and decreased thermal boundary layer. The temperature generated a similar effect, increasing average efficiency from 9–10% at 30 °C to ~16% at 90 °C, the performance was further influenced by improved thermal driving. On the other hand, sand bulk had a non-monotonic response with optimal performance: 200 g enhanced an efficiency (≈13.5–13.6%) while both low (100 g) and high (300 g) loads decreased efficiency, due to insufficient heat transfer area and too high hydrodynamic resistance, respectively. Collectively results ensure the best trade-off between enhanced mixing and limited entrance-loss is achieved by the Ring inlet, thus allowing the maximization of heat transfer and electrical recovery. Thus, the ideal operating window of the current system is high inflow (approx. 1.5 m/s) with elevated thermal environment (≈ 90 °C) and moderate sand loading (approx. 200 g) where the reactor reaches its full efficiency (~ 27–28%) and power output (~ 3.5 W). Such discoveries solidify inlet layout is a decisive factor, that could increase the efficiency (electrical output) by over 25% with identical conditions and provide a practical basis for optimizing compact thermo-fluid energy conversion plants.

Further investigations should broaden the present experimental framework to investigate a wider range of airflow and temperature conditions, and to study the system performance under more severe working conditions. The effect of additional granular materials and particle sizes on heat transfer and pressure drop should also be investigated for the development of the thermal storage and fluidization profile. Moreover, combining several thermoelectric units or hybrid energy recovery stages could result in an outstanding increase in electrical output. Sophisticated inlet geometry inspired inlet developments based on bio-inspired and vortex-generating geometries may further enhance the uniformity and mixing efficiency of flows. Lastly, integrating experimental measurements with numerical CFD modeling would allow a significant correlation between the internal flow structures and thermal fields in detail to better understand the structure within the inside flow and to offer predictive management of optimized compact thermo–fluid energy conversion systems.

Nomenclature

Symbol	**Description**	**Unit**	
A_c	Cross-sectional area of acrylic reactor column	m^2	
$c_{p,a}$	Specific heat capacity of air	$J \cdot kg^{-1} \cdot K^{-1}$	
$C_{\Delta P}$	Pressure drop coefficient	-	
D	Inner diameter of acrylic column	m	
d_p	Mean sand particle diameter	m	

I	Electrical current generated	A	
P_e	Electrical power output	W	
P_k	Kinetic power of airflow	w	
P_{in}	Inlet pressure	Pa	
P_{out}	Outlet pressure	Pa	
Q	Volumetric airflow rate	$\text{m}^3 \cdot \text{s}^{-1}$	
$\dot{Q}_{\text{th}}$	Thermal power transferred from airflow	W	
R	Electrical load resistance	Ω	
Re	Reynolds number	-	
Re_p	Particle Reynolds number	-	
T_{in}	Inlet air temperature	℃ or K	
T_{out}	Outlet air temperature	℃ or K	
v	Superficial air velocity	$\text{m} \cdot \text{s}^{-1}$	
V	Electrical voltage generated	V	
$\dot{m}_a$	Mass flow rate of air	$\text{kg} \cdot \text{s}^{-1}$	
ΔP	Pressure drop across sand bed	Pa	
η	Thermal-to-electrical efficiency	%	
η_k	Kinetic-to-electrical efficiency	%	
ρ_a	Density of air	$\text{kg} \cdot \text{m}^{-3}$	
μ_a	Dynamic viscosity of air	Pa-s	
ϵ	Energy balance residual	%	

References

[1] Abdelmagied, M. (2024). Thermo-fluid characteristics and exergy analysis of a twisted tube helical coil. *Sci Rep*, *14*(1), 27873. https://doi.org/10.1038/s41598-024-78164-1

[2] Abdelrehim, O., Awad, A. M., Hegazi, A. A., El-Said, E. M. S., & Khater, A. (2024). Innovative enhancements in solar still performance: A comprehensive study on wick-absorber configurations. *Case Studies in Thermal Engineering*, *63*. https://doi.org/10.1016/j.csite.2024.105273

[3] Acharya, S., Karanth, K. V., Kumar, S., & H. S., A. (2025). Thermo-fluid analysis of a spring fin turbulator placement on the absorber plate of the solar air heater. *International Journal of Thermofluids*, *30*. https://doi.org/10.1016/j.ijft.2025.101444

[4] Agati, G., Franchetti, B., Rispoli, F., & Venturini, P. (2024). Thermo-fluid dynamic analysis of the air flow inside an indoor vertical farming system. *Applied Thermal Engineering*, *236*. https://doi.org/10.1016/j.applthermaleng.2023.121553

[5] Alrashidi, A., Abdo, S., Abdelrahman, M. A., Altohamy, A. A., & Elsemary, I. M. M. (2025). Investigating the effectiveness of hydrogels for PV cooling across different operational conditions: An

experimental approach. *Case Studies in Thermal Engineering*, *75*. https://doi.org/10.1016/j.csite.2025.107125

[6] Atiqur Rahman, M., Mozammil Hasnain, S. M., & Zairov, R. (2025). Thermo-Hydraulic Performance of Tubular Heat Exchanger with Opposite-Oriented Trapezoidal Wing Perforated Baffle Plate. *Tehnički glasnik*, *19*(3), 350-358. https://doi.org/10.31803/tg-20230928070645

[7] Baccoli, R., Di Meglio, A., Fenu, A., & Massarotti, N. (2025). Design and performance of a ThermoAcoustic Electric Generator powered by waste-heat based on linear and nonlinear modelling. *Applied Thermal Engineering*, *276*. https://doi.org/10.1016/j.applthermaleng.2025.126938

[8] Behzad, M., Poncet, S., & Sarmiento-Laurel, C. (2025). Multi-objective optimization on thermo-structural performance of honeycomb absorbers for concentrated solar power systems. *Case Studies in Thermal Engineering*, *70*. https://doi.org/10.1016/j.csite.2025.106068

[9] Bianco, N., Fragnito, A., Iasiello, M., & Mauro, G. M. (2023). A CFD multi-objective optimization framework to design a wall-type heat recovery and ventilation unit with phase change material. *Applied Energy*, *347*. https://doi.org/10.1016/j.apenergy.2023.121368

[10] Catalán-Martínez, D., Navarrete, L., Tarach, M., Santos-Blasco, J., Vøllestad, E., Norby, T.,…Serra, J. M. (2022). Thermo-fluid dynamics modelling of steam electrolysis in fully-assembled tubular high-temperature proton-conducting cells. *International Journal of Hydrogen Energy*, *47*(65), 27787-27799. https://doi.org/10.1016/j.ijhydene.2022.06.112

[11] Claussner, L. M., Scarponi, G. E., & Ustolin, F. (2025). Thermo-Fluid Dynamics Modelling of Liquid Hydrogen Storage and Transfer Processes. *Hydrogen*, *6*(4). https://doi.org/10.3390/hydrogen6040122

[12] Dhaundiyal, A., & Atsu, D. (2022). The effect of thermo-fluid properties of air on the solar collector system. *Alexandria Engineering Journal*, *61*(4), 2825-2839. https://doi.org/10.1016/j.aej.2021.08.015

[13] Di Meglio, A., & Massarotti, N. (2022). CFD Modeling of Thermoacoustic Energy Conversion: A Review. *Energies*, *15*(10). https://doi.org/10.3390/en15103806

[14] Di Meglio, A., Massarotti, N., & Piccolo, A. (2024). Experimental validation of a heat exchanger model for thermoacoustic applications. *Journal of Physics: Conference Series*, *2685*(1). https://doi.org/10.1088/1742-6596/2685/1/012014

[15] Fu, Y., Shan, G., Zhang, X., Zhao, L., & Yang, Y. (2025). Design and Fabrication of Embedded Microchannel Cooling Solutions for High-Power-Density Semiconductor Devices. *Micromachines (Basel)*, *16*(8). https://doi.org/10.3390/mi16080908

[16] Guille, A., Mohankumar, M. B., Hampel, U., & Unger, S. (2026). Thermo-fluid and economic performance of PCHEs in a high-temperature thermal energy storage system coupled with an sCO2 Brayton cycle. *International Journal of Heat and Mass Transfer*, *256*. https://doi.org/10.1016/j.ijheatmasstransfer.2025.127918

[17] Jiao, K., Ma, B., Liu, X., Chen, B., Wang, Q., & Zhao, C. (2024). Advances in 3D Materials-Based Hydrovoltaic Generators and Synergistic Energy Conversion. *ChemElectroChem*, *11*(20). https://doi.org/10.1002/celc.202400330

[18] Kwasi-Effah, C. C., Ibhadode, O., & Qureshi, A. (2024). Thermo-hydraulic performance characteristics of novel G-Prime and FRD Triply Periodic Minimal Surface (TPMS) geometries. *International Communications in Heat and Mass Transfer*, *159*. https://doi.org/10.1016/j.icheatmasstransfer.2024.108226

[19] Mezzacapo, A., D'Addio, R., & De Stefano, G. (2025). A Computational Thermo-Fluid Dynamics Simulation of Slot Jet Impingement Using a Generalized Two-Equation Turbulence Model. *Energies*, *18*(14). https://doi.org/10.3390/en18143862

[20] Persico, G., Romei, A., Gaetani, P., Bellobuono, E. F., Toni, L., & Valente, R. (2024). Thermo-fluid dynamic modeling of a supercritical carbon dioxide compressor for waste heat recovery applications. *Energy*, *294*. https://doi.org/10.1016/j.energy.2024.130874

[21] Rahman, M. A. (2024a). Thermo-fluid performance of a heat exchanger with a novel perforated flow deflector type conical baffles. *Journal of Thermal Engineering*, 868-879. https://doi.org/10.14744/thermal.0000846

[22] Rahman, M. A. (2024b). Thermo-fluid performance of axially perforated multiple rectangular flow deflector-type baffle plate in an tubular heat exchanger. *Applications in Engineering Science*, *20*. https://doi.org/10.1016/j.apples.2024.100197

[23] Rostami, S., & Ahmadi, N. (2025). In the Study of the Effects of the Pipe Design of a Heat Exchanger on the Thermo-Fluid Characteristics and Exergy Destruction. *Processes*, *13*(3). https://doi.org/10.3390/pr13030835

[24] Sahrane, S., & Niou, S. (2025). Evaluating turbulence models for accurate thermo-fluid

simulation in sthe with combined tube bundles. *Turkish Journal of Engineering*, *9*(2), 258-271. https://doi.org/10.31127/tuje.1546393

[25] Sarkar, S. (2024). Computational Thermo-Fluid Dynamics Modeling for Process Optimization in Hydrogen-Integrated Industrial Heat Systems. *Journal of Sustainable Development and Policy*, *03*(03), 87-133. https://doi.org/10.63125/8rm6bc88

[26] Shimada, Y., Watanabe, N., Ueno, A., & Nagano, H. (2024). Evaluation of evaporative heat transfer performance based on observation of Thermo-Fluid behavior in porous structures fabricated by additive manufacturing. *Thermal Science and Engineering Progress*, *56*. https://doi.org/10.1016/j.tsep.2024.103081

[27] Starace, G., Falcicchia, L., Panico, P., Fiorentino, M., & Colangelo, G. (2021). Experimental performance comparison between circular and elliptical tubes in evaporative condensers. *Journal of Thermal Analysis and Calorimetry*, *147*(11), 6363-6373. https://doi.org/10.1007/s10973-021-10968-z

[28] Toor, Z., Bahaidarah, H. M., Zayed, M. E., Rehman, S., Khanna, V., & Shalaby, S. M. (2026). Experimental investigation and CFD modeling on rooftop vertical axis wind turbine for sustainable residential buildings: development of core design optimization and advanced performance analysis. *Energy and Buildings*, *353*. https://doi.org/10.1016/j.enbuild.2025.116901

[29] Xiao, Y., Wu, X., Tong, X., Chen, E., & Zhang, C. (2025). Reproducible Thermo-Fluid–Solid-Coupled Modeling of Wet Milling of Al6061: Parametric Influence and Surface Integrity Assessment. *Metals*, *15*(11). https://doi.org/10.3390/met15111256